Scientific Reports

https://doi.org/10.1038/s41598-026-35821-x

Article in Press

Synthesis of carbon-supported multimetallic palladium-based electrocatalysts for direct ethanol fuel cells (DEFCs)

Received: 9 July 2025

Accepted: 8 January 2026

Published online: 16 February 2026

Cite this article as: ElSheikh A., Alsoghier H.M., Mousa H.M. *et al.* Synthesis of carbon-supported multimetallic palladium-based electrocatalysts for direct ethanol fuel cells (DEFCs). *Sci Rep* (2026). https://doi.org/10.1038/s41598-026-35821-x

Ahmed ElSheikh, Hesham M. Alsoghier, Hamouda M. Mousa, Chunyu Zhu & James McGregor

Synthesis of Carbon-Supported Multimetallic Palladium-based Electrocatalysts for Direct Ethanol Fuel Cells (DEFCs)

Ahmed ElSheikh[a,b,*], Hesham M. Alsoghier[c], Hamouda M. Mousa[b,] Chunyu Zhu[d], James McGregor[a]

[a] Department of Chemical & Biological Engineering, University of Sheffield, Sheffield S1 3JD, United Kingdom
[b] Mechanical Engineering Department, Faculty of Engineering, Qena University, Qena 83523, Egypt
[c] Chemistry Department, Faculty of Science, Qena University, Qena 83523, Egypt
[d] School of Low-Carbon Energy and Power Engineering, China University of Mining and Technology, Xuzhou, 221116, China
*Corresponding Author: ahmed.elsheikh@eng.svu.edu.eg,

Abstract

The commercialization of direct ethanol fuel cells (DEFCs) is hindered by platinum dependency, catalyst degradation, and high costs. This work addresses these challenges by developing carbon-supported trimetallic PdAuM/C (M = Rh, Ir, Ag) electrocatalysts for the ethanol oxidation reaction (EOR). Through a controlled synthesis protocol, PdAuM/C nanoparticles (3.1–6.7 nm) with alloyed structures were characterized by XRD, TEM, EDX, and XPS. Electrochemical analyses (CV, CA, EIS) in alkaline media revealed unprecedented EOR activity: PdAuRh/C achieved a peak current density of 10,500 $mA \cdot mg^{-1}_{Pd}$ and onset potential of −680 mV vs. NHE—5.8× higher current and 195 mV lower overpotential than monometallic Pd/C (1,800 $mA \cdot mg^{-1}_{Pd}$, −485 mV). PdAuIr/C and PdAuAg/C also outperformed Pd/C, though PdAuAg exhibited atypical dual oxidation peaks. The synergistic electronic effects in PdAuRh/C minimized CO poisoning and maximized active sites, positioning it as a sustainable, high-performance alternative to Pt-based catalysts for DEFCs.

Keywords: Ethanol oxidation reaction (EOR), trimetallic electrocatalysts, Palladium-gold catalysts, Alkaline electrocatalysis

1. Introduction

The urgent demand for clean energy alternatives to fossil fuels has intensified owing to the escalating threats of climate change. Direct ethanol fuel cells (DEFCs), which electrochemically convert ethanol chemical energy into electricity without direct carbon emissions during operation, represent a sustainable pathway for eco-friendly power generation. Bioethanol, a fuel source for DEFCs, is derived from renewable biomass, positioning DEFC technology as a carbon-neutral energy solution [1, 2]. However, DEFC commercialization faces two major challenges: (1) catalyst deactivation caused by adsorbed CO-like intermediates, which drastically reduces catalytic durability, and (2) kinetically and thermodynamically unfavorable cleavage of the ethanol molecule-robust C–C bond. In-situ analyses of the ethanol oxidation reaction (EOR) on Pt- and Pd-based electrocatalysts revealed a dominant C2 pathway, wherein acetic acid is produced without C–C bond scission, as opposed to the C1 pathway, which fully oxidizes ethanol to CO_2 [9, 14, 19, 39, 65]. This preference for the C2 pathway limits the electrical efficiency to 33% of its theoretical maximum (four electrons transferred per ethanol molecule versus 12 electrons in the C1 pathway). Although platinum exhibits superior catalytic activity for EOR, its scarcity, high cost, and vulnerability to CO poisoning impede its viability for large-scale DEFC applications. Thus, palladium has emerged as a promising Pt alternative, demonstrating comparable catalytic performance while exhibiting enhanced resistance to CO-induced poisoning [6, 30].

Furthermore, active metal nanoparticles require dispersion onto an inert, conductive, and mesoporous support with a high surface area, such as carbon black [3, 13, 49]. The support provides mechanical stability, enhances the electrochemically active surface area, and prevents

nanoparticle agglomeration. To optimize the electrocatalytic activity of palladium toward the ethanol oxidation reaction (EOR), the incorporation of a secondary transition metal has been shown to modulate the Pd electronic structure, refine its crystal lattice, and tailor its morphological properties. Notable examples of transition metals that synergistically enhance Pd-based EOR catalysts include gold [17, 22, 29, 41, 52, 59], nickel [25, 43, 61, 66], cobalt [23,24], silver [4, 20, 40, 56, 57], rhodium [31], iridium [5, 34, 46, 47], and tin [21, 32, 50].

PdAu-based electrocatalysts have been extensively reported for direct alcohol oxidation. Qin et al. [42] have prepared carbon-nanofiber-supported PdAu electrocatalysts and applied them for formic acid oxidation. They have found enhanced electrocatalytic performance of PdAu samples due to strong alloying between Pd and Au. They have found that the high-alloying method utilizing a tetrahydrofuran-water (THF-H_2O) solution achieves a better alloying degree in the resulting Pd-Au system compared to an only water solution. A similar finding was obtained by [53, 62]. Using a similar approach while replacing CNF with functionalized MWCNT, Zhang et al. [63] synthesized PdAu electrocatalysts, with varying Pd:Au atomic ratios, for formic acid oxidation. They have found the best Pd:Au ratio to be 4:1. Chen et al. [8] chose to electrochemically dealloy the $Pd_{20-y}Au_yNi_{80}$ ternary alloy to produce unsupported PdAu electrocatalysts. In contrast to the previous studies, Feng et al. [18] have found that the best Pd:Au ratio for ethanol oxidation reaction is 1:1. However, Dutta et al. [11] have found the best performing PdAu composition for ethanol oxidation is the $Pd_{67}Au_{33}$ one. Using the electron beam irradiation to prepare Pd_xAu_y/C ethanol electrocatalysts, Geraldes et al.[23] have found a comparable and superior EOR performance of both $Pd_{50}Au_{50}$ and $Pd_{90}Au_{10}$. Compared to ethanol, methanol oxidation on PdAu systems was reported using multiple Pd_xAu_y/C nanocatalysts, and the highest-performing one is the $Pd_{30}Au_{70}$ [60].

Despite the growing interest in bimetallic catalysts, only limited research has focused on enhancing their performance by incorporating a third metal. Trimetallic systems such as PdAuNi [10, 15, 51], PdAgNi [13, 55], PdIrNi [45], and PdNiSn [44] have demonstrated enhanced ethanol oxidation reaction (EOR) activity, although the outcomes vary depending on compositional and structural factors. Given the established role of Au as an effective cocatalyst for Pd-based systems, this study introduces the first reported investigation of PdAu-based trimetallic electrocatalysts alloyed with Rh, Ir, or Ag for EOR applications. These three cocatalysts are chosen based on their verified enhancement of the EOR on the Pd surface in the case of the binary systems [4, 20, 40, 56, 57]. This study is a proof-of-concept investigation of how alloying Pd with Au and a third metal (Rh, Ir, Ag) affects EOR kinetics and poisoning resistance. The objective is to identify compositions that deliver substantially higher intrinsic activity and/or stability, which can then guide the development of lower-cost formulations

2. Experimental

2.1. Materials

The chemical reagents used in this study were palladium(II) chloride (99 wt. %), gold(III) chloride ($AuCl_3$, 99 wt.%), silver nitrate ($AgNO_3$, 97 wt.%), iridium(III) chloride ($IrCl_3$, 98 wt.%), potassium bromide (KBr, 95 wt.%), potassium hydroxide (KOH, 85 wt.%), ethanol (99 wt.%), and 2-propanol (99 wt.%), all of which were acquired from Sigma-Aldrich. Commercial Vulcan carbon (Brunauer–Emmett–Teller (BET) surface area: 230 m^2/g; pore size: 19 nm; pore volume: 0.25 cm^3/g) was obtained from Cabot Corporation. Four catalysts were synthesized for comparative analysis: three carbon-supported trimetallic systems (PdAuAg/C, PdAuIr/C, and PdAuRh/C) and a monometallic Pd/C catalyst. The preparation involved combining metal precursors with the

carbon support at molar ratios of Pd:Au:M (M = Ag, Ir, Rh) fixed at 1:1:1. The precise quantities of metal salts and carbon used for catalyst fabrication are listed in Table 1.

Table 1 Stochiometric quantities of C, $PdCl_2$, $PdAuCl_3$, $AgNO_3$, $RhCl_3$, and $IrCl_3$ to prepare Pd/C. PdAuAg/C, PdAuIr/C, and PdAuRh/C, respectively:

Catalyst	C	$PdCl_2$		$AuCl_3$		$AgNO_3$		$RhCl_3$		$IrCl_3$	
	(mg)	mg	mmol	mg	mmol	mg	mmol	mg	mmol	mg	mmol
Pd/C	132	30	0.282	-	-	-		-		-	-
PdAuAg/C	132	6.76	0.038	15.88	0.052	6.76	0.039	-	-	-	-
PdAuIr/C	132	6.41	0.036	10.90	0.036	-	-	-	-	10.28	0.034
PdAuRh/C	132	7.80	0.044	13.33	0.044	-	-	9.26	0.044	-	-

*Theoretical metal loading: 12 wt.% for all catalysts

2.2. Methods

Catalyst synthesis followed a modified protocol adapted from prior methodologies [33,45]. Initially, the metal precursor and Vulcan carbon support were homogenously dispersed in a 2-propanol/deionized water solution (1:1 volume/volume ratio) under vigorous stirring for 10 min. Subsequently, potassium bromide (KBr) was introduced at a molar ratio of 1.5 relative to the total metal content across all catalyst formulations. KBr was added to act as a capping agent, which is achieved through the anion exchange method with the larger Br^- ion potentially replacing the smaller Cl^- ion. Then, the Br^- would surround the metal nanoparticles and act as a capping agent. A freshly prepared aqueous sodium borohydride solution (0.5 M, 15 mL) was then incrementally added to the mixture, which was maintained under continuous agitation for 30 min to ensure complete reduction. The resulting solid product was isolated via vacuum filtration, thoroughly

rinsed with deionized water to remove residual impurities, and finally dried at 80 °C for 12 hours in a vacuum oven. All catalysts were prepared with a nominal total metal loading of ≈12 wt% (metals : carbon by mass ≈ 0.12 : 0.88), i.e., ~12 wt% total metal supported on Vulcan XC-72. The exact precursor masses used to achieve these nominal loadings are given in Table 1. The EDX-determined total metal contents are reported in (PdAuAg/C and PdAuRh/C ≈11.95 wt%, PdAuIr/C ≈8.65 wt%).

2.3. Catalyst Characterization

The elemental composition of the catalyst surfaces was determined using Energy-Dispersive X-ray spectroscopy (EDX) coupled with a JEOL JSM-6010LA Scanning Electron Microscope (SEM). Crystalline phase analysis was conducted via X-ray Diffraction (XRD) on a Bruker D2 Phaser diffractometer equipped with Cu Kα radiation (λ = 0.1540 nm), operated at 30 kV and 10 mA. Morphological features were investigated using transmission electron microscopy (TEM) on a Philips CM100 instrument fitted with a Lanthanum Hexaboride (LaB_6) filament and operated at an accelerating voltage of 100 kV. This instrument is unable to produce HRETM and lattice-fring imaging. X-ray photoelectron spectroscopy (XPS) probed the chemical states using a Thermo Scientific K-Alpha+ spectrometer with a monochromatic Al Kα X-ray source (72 W). Survey scans and high-resolution spectra were acquired at pass energies of 140 eV and 50 eV, respectively. The background subtraction method is Shirley. Fitting function was accomplished via Gaussian–Lorentzian mixed peaks. The spin-orbit splitting and area constraints for Pd 3d ($3d_{5/2}$: $3d_{3/2}$ = 3:2), and the energy separation used for the two components. Electrochemical Measurements

The electrocatalytic activities of the synthesized materials toward the Ethanol Oxidation Reaction (EOR) were evaluated using Cyclic Voltammetry (CV), Chronoamperometry (CA), and Electrochemical Impedance Spectroscopy (EIS). The experiments were conducted in a three-

electrode cell configuration interfaced with a Gamry Reference 600 potentiostat. An Ag/AgCl electrode (saturated KCl) served as the reference electrode, while a platinum wire acted as the counter electrode. It should be noted that Ag/AgCl is not suitable for long-term alkaline tests due to the chloride leakage potential. Yet, for the reported short-term test, chloride leakage is minimized. Reversible hydrogen electrode or Hg/HgO is a better potion as a reference electrode in alkaline electrolytes. All potentials are reported relative to the normal hydrogen electrode (NHE). The working electrode was a polished glassy carbon electrode (GCE, 3 mm in diameter) modified by depositing a catalyst ink. This ink was prepared by ultrasonically dispersing 5 mg of the catalyst powder in a solution containing 2000 μL of ethanol and 25 μL of Nafion® 117 binder (5 wt.% %) for 1 hour. A 25 μL aliquot of the homogeneous slurry was drop-cast onto the GCE surface, resulting in a total Pd mass loading of 85 μg/cm². Before coating, the GCE was sequentially polished with 1 μm and 0.05 μm alumina suspensions to ensure a mirror-like surface.

CV and CA measurements were performed in a stirred electrolyte (50 rpm) to mitigate mass transport losses. We acknowledge CA tests were conducted at fixed potentials of −0.3 V and +0.1 V (vs. NHE), with the current densities normalized to the Pd mass. For EIS, the electrolyte was maintained in a quiescent state to minimize noise interference. Impedance spectra were recorded over a frequency range of 10 kHz to 0.1 Hz with a 5 mV AC amplitude, preceded by a 10-minute potentiostatic hold to stabilize the open-circuit potential.

3. Results and discussions

3.1. XRD Analysis

Fig. 1 displays the X-ray diffraction (XRD) patterns of the synthesized Pd/C, PdAuAg/C, PdAuIr/C, and PdAuRh/C catalysts (*left*) and their respective enlarged (111) facets (*right*). A broad diffraction feature centered at ~25° is observed for all samples, consistent with the semi-crystalline

structure of the Vulcan carbon support. For the monometallic Pd/C catalyst, distinct Bragg reflections corresponding to the (111), (200), (220), and (311) crystallographic planes of face-centered cubic (*fcc*) palladium are identified at 39.8°, 46.0°, 67.7°, and 82.2°, respectively (JCPDS No. 46-1043). Table 2 lists the interplane distance (d_{111}, Å), calculated according to Bragg's law, lattice constant (*a*, Å), and crystallite size (L, nm) calculated using Scherrer's equation. The overlapping peaks, particularly in PdAuRh/C and PdAuAg/C, were deconvoluted to ensure a more accurate assessment of d_{111}, *a*, and L. For the monometallic Pd/C, the estimated values of d_{111} and a are 2.26 and 3.91 Å, respectively, while the crystallite size is 3.38 (Table 2). In the trimetallic systems, the diffraction peaks are shifted to angles intermediate between pure Pd (JCPDS 46-1043) and pure Au (JCPDS 04-0784), as illustrated in Fig. 1 (*left*). Notably, the PdAuIr/C pattern exhibits a single set of diffraction peaks for Pd, Au, and Ir at each crystallographic orientation, indicative of alloy formation. These reflections are shifted by approximately 0.5° (Table 2) toward lower diffraction angles relative to those of monometallic Pd, approaching the lattice parameters of Au. This negative shift suggests the substitutional incorporation of Au and Ir atoms into the Pd *fcc* lattice, forming a ternary solid-solution alloy, a phenomenon corroborated by prior reports [46].

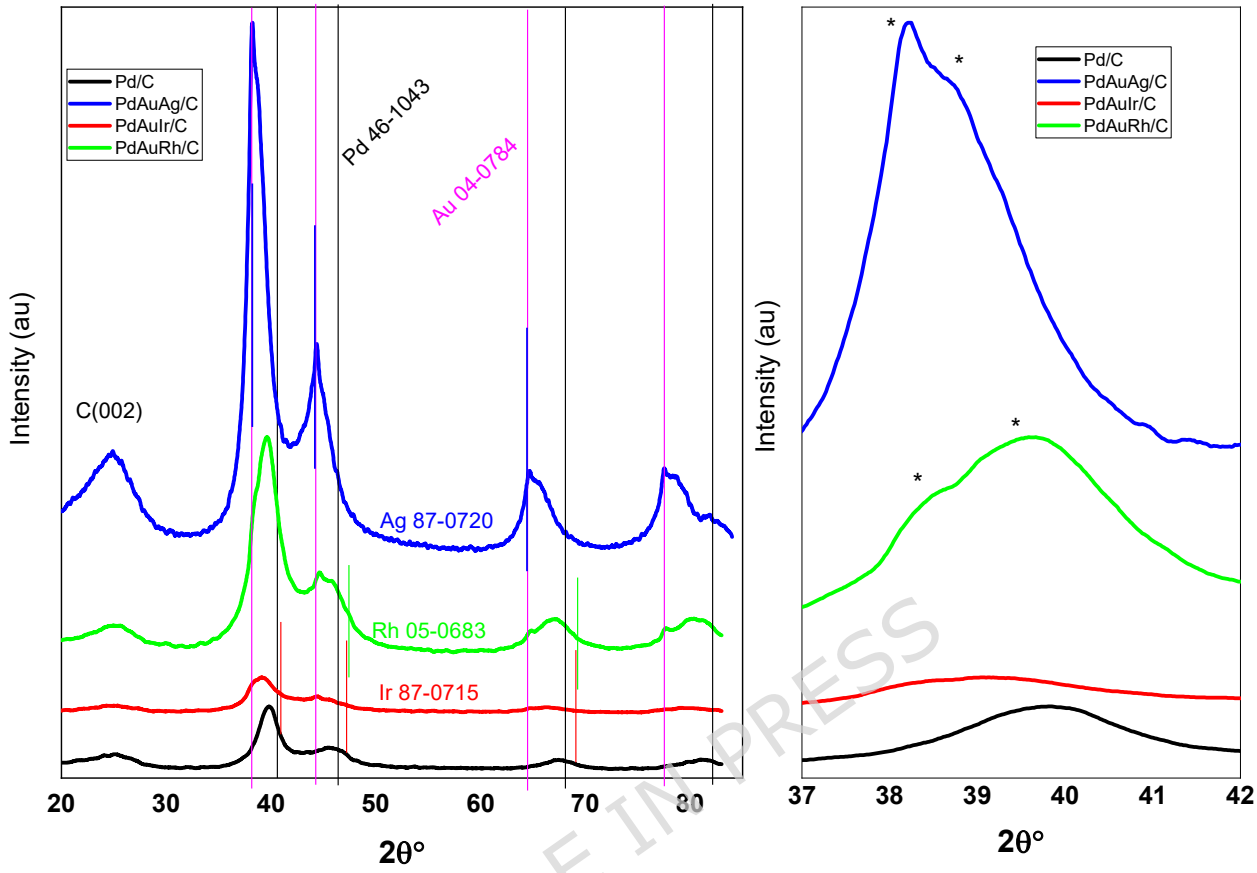

Fig. 1 (Left) X-ray diffraction (XRD) patterns of Pd/C, PdAuAg/C, PdAuIr/C, and PdAuRh/C, (Right) enlarged (111) facet

Table 2 The main reflection (111) data of Pd/C, PdAuRh/C, PdAuIr/C, and PdAuAg/C

Catalyst	2θ°	d_{111} (Å)	*a* (Å)	Lattice shift°	Crystallite size L (nm)
Pd/C	39.8	2.26	3.91	0	3.38
PdAuRh/C	39.6	2.27	3.93	-0.2	2.81
PdAuIr/C	39.3	2.28	3.95	-0.5	2.34
PdAuAg/C	38.6	2.33	4.03	-1.2	4.34

The resulting PdAuIr/C system ehibits a single phase of a ternary PdAuIr alloys system with no visible peak overlapping unlike previous report [33] of PdAuIr catalysts with varying atomic ratios (Pd:Au:Ir = 18:1:1, 7:2:1, and 10:9:1). The Pd-rich composition ($Pd_{18}Au_1Ir_1$) exhibited a single-phase XRD pattern consistent with a Pd-Au alloy, whereas the other two ratios demonstrated phase separation into Pd-rich and Au-rich domains. For the current PdAuIr/C system, the values of d_{111}

and a are 2.28 Å and 3.95 Å, respectively, while the crystallite size is 2.34 nm. This suggests adding Au and Ir to Pd/C slightly elongates the lattice and decreases the crystal size. For the PdAuAg/C catalyst, the diffraction peaks display the largest shift (1.2°) toward lower angles (Table 2), potentially attributed to the Ag- and Au-rich phase, both of which exhibit lower diffraction angles than Pd, as demonstrated by their diffraction patterns. The overlapping peaks further confirm this (Fig. 1-right). This trend aligns with [38], which documented progressive peak shifts with increasing Au and Ag contents. The near-identical reflections of Au and Ag—observed at 38.2° (111), 44.4° (200), 64.6° (220), and 77.4° (311) further complicate the phase distinction in PdAuAg systems. Ulas et al. [55] reported analogous behavior in PdAg and PdAgNi catalysts, noting single-phase Pd-Ag alloys in bimetallic systems, but distinct Pd-derived shoulder peaks in trimetallic compositions with 30–50% Ag. The d_{111} and a values of PdAuAg/C are 2.33 and 4.03 Å, while the crystal size is 4.34 nm (Table 2). This suggests adding Au and Ag to Pd/C increases the interplane distance, elongates the lattice, and increases the crystal size. It is noteworthy that full Rietveld refinement or high-quality powder patterns (and/or synchrotron data) would allow more rigorous extraction of lattice parameters and phase fractions.

Similar to PdAuAg/C, the intermetallic PdAuRh/C system shows overlapping peaks visibale in Fig. 1 (right). These are similar to overlapping patterns observed in [38, 58]. The d_{111} and *a* values of the PdAuRh/C system are 2.27 and 3.93 Å, while the crystal size is 2.81 nm (Table 2). This suggests that adding Au and Rh to Pd/C slightly elongates the lattice (lattice shift 0.2° only) but significantly decreases the crystal size. This divergence suggests that PdAuIr forms a homogeneous ternary alloy, whereas PdAuRh and PdAuAg exhibit partial phase segregation. Comparatively, Dutta et al. [12] synthesized PdAu/C catalysts under analogous conditions and

observed fully resolved Pd and Au peaks, attributing this to coexisting Au- and Pd-rich phases—a finding corroborated by [41].

3.2. EDX Analysis

Table 3 lists the EDX-obtained data of metal atomic ratios and composition of PdAuAg/C, PdAuIr/C, and PdAuRh/C. Even though the theoretical Pd:Au:M ratio is 1: 1: 1, only PdAuIr/C ratio meets that ratio. For PdAuRh/C and PdAuAg/C, the proportions have shown higher Au concentrations and lower M (Rh, Ag) ones than Pd. The potential reasons for this divergence are the metal surface chemistry and EDX electron beam penetration depth which changes following the accelerating voltage. The EDX results are shown in the Supplementary material (Table S1 and Fig. S.1). PdAuIr/C has a 1:1:1: atomic ratio of the three metals, but the total metal load, unlike PdAuAg/C and PdAuRh, is 3% lower than the theoretical value of 12 wt.%. While the total metal loadings were estimated from precursor stoichiometry and verified by EDS, we acknowledge that thermogravimetric analysis (TGA) under oxidative conditions would provide a more accurate quantification, and we recommend it for future follow-up studies.

Table 3 EDX elemental Mtal atomic ratio and composition of PdAuAg/C, PdAuIr/C, and PdAuRh/C at 20 kV

Catalyst	Pd:Au:M ratio	**Pd**		**Au**		**Ag**		**Ir**		**Rh**		Tot. Wt. %	Nominal wt% on C
		wt.%*	at. %**	wt. %	at. %	wt. %	at. %	wt. %	at. %	wt. %	at. %		
PdAuAg/C	4:5:2	3.11	0.41	6.95	0.49	1.88	0.24	-	-	-	-	11.95	12
PdAuIr/C	1:1:1	1.87	0.24	3.41	0.24	-	-	3.37	0.24	-	-	8.65	12
PdAuRh/C	4:5:3	2.94	0.40	6.47	0.47	-	-	-	-	2.45	0.34	11.95	12

wt. %: weight concentration percentage
**at. %: molar concentration percentage

Fig. 2 shows the EDX elemental maps (Pd, Au, M) of the three intermetallic catalysts recorded at 20 kV. A high level of metal mixing could be observed by looking at any three maps of any particular sample.

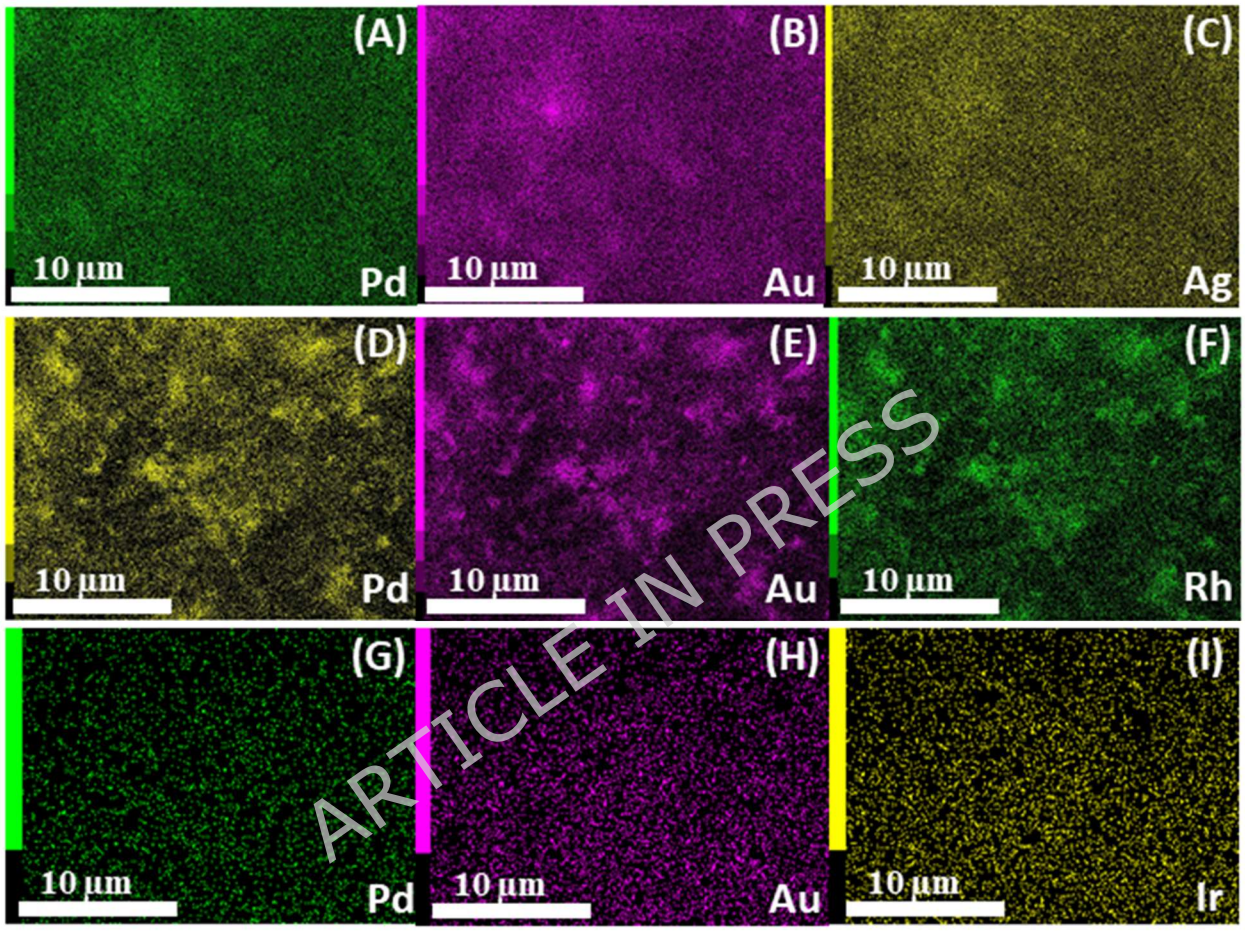

Fig. 2 EDX elemental maps of PdAuAg/C (A, B, C), PdAuRh/C (D, E, F), and PdAuIr (G, H, I) recorded at 20 kV

3.3. TEM Analysis

Fig. 3 shows the morphological analysis of the samples. For each catalyst, 100 randomly selected particles were used to estimate the average particle size. The carbon aggregates (30-60 nm) appeared gray in all sample micrographs. For Pd/C (Fig. 3. a, b), semi-spherical dark metal

nanoparticles were observed to spread over the gray carbon aggregates. However, some segments of agglomerated Pd particles could also be observed.

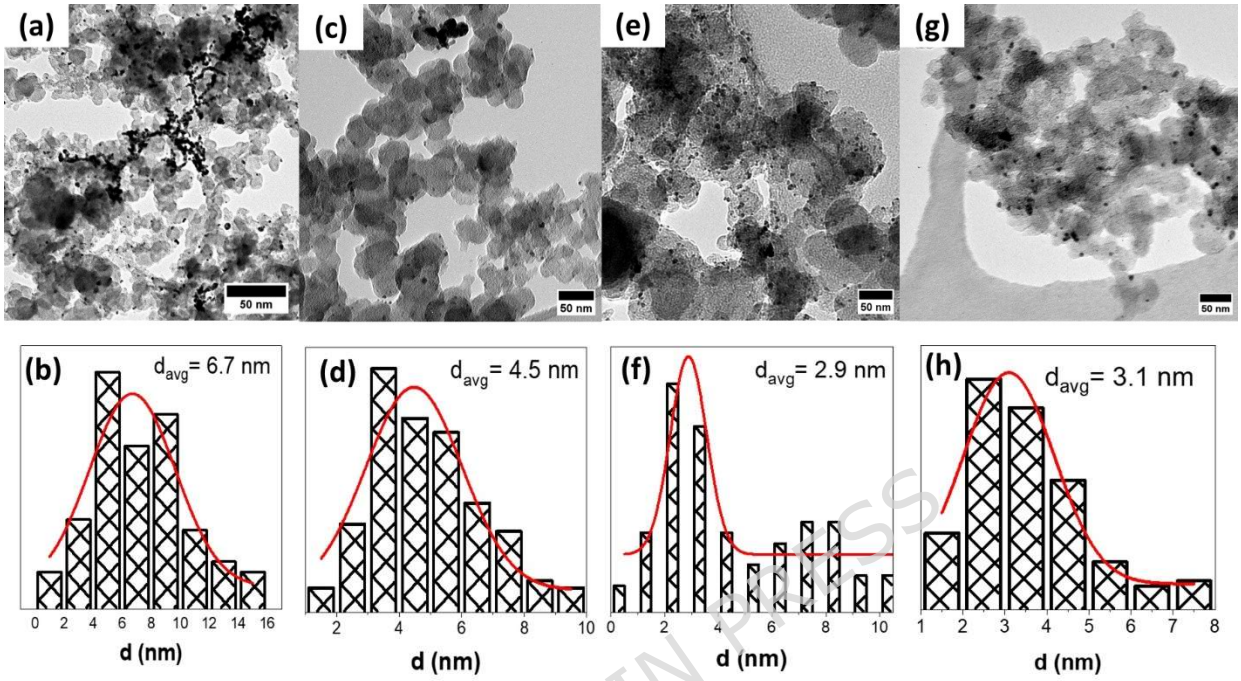

Fig. 3 Transmission electron microscopy (TEM) micrographs and particle size distribution of Pd/C (a,b), PdAuAg/C (b,c), PdAuIr/C (e, f), PdAuRh/C (g,h)

The average particle size of Pd was 6.7 nm. For PdAuAg, Fig. 3. c, d show a reduction in the particle size compared to Pd/C that has been confirmed for PdAuAg vs. PdAg in [58]. The average PdAuAg size is 4.5 nm, which is 1.3 nm higher than that of [16]. TEM particle sizes exceed XRD crystallite sizes due to polycrystallinity or aggregation. The particle size of PdAuIr (Fig. 3. e, f) is smaller than that of Pd and PdAuAg. The average PdAuIr particle size is the smallest (2.9 nm) among the four samples. Contrary to Neto et al. [33], who observed larger PdAuIr particles than Pd. No significant difference between the particle sizes of Pd, PdIr, and PdAuIr samples prepared in [46] was noted. Slightly higher particle agglomeration than PdAuIr is noted by looking at the PdAuRh micrograph (Fig. 3. g, h). The average particle size of the PdAuRh (Fig. 3. h) is higher than

that of PdAuIr, but still lower than those of PdAuAg and Pd. The metal particle size obtained for the current samples is relatively small, which suggests increased Pd active site density and, therefore, enhanced electrochemical active surface area (ECSA) and electrocatalytic performance [10, 16, 22, 27, 38, 41, 58]. It is noteworthy that the particle size of PdAuAg/C (4.5 nm) is larger than that of PdAuRh/C and PdAuIr/C (4.4 and 3.6 nm). The XRD crystal size for Pd/C, PdAuRh/C, PdAuAg/C, and PdAuIr/C is 3.38, 2.81, 4.34, and 2.34 nm. These values are slightly smaller than those of the assessed TEM average particle size of 6.7, 3.1, 4.5, and 2.9 nm. This agrees with the general findings of XRD since both Ag and Au geometries (lattice structure) are larger than that of Pd.

3.4. XPS analysis

The metal valence states and surface compositions were examined using X-ray photoelectron spectroscopy (XPS). Fig. 4 (a, b, c, d, e, f) show the XPS peaks of Pd 3d on Pd/C, C 1s, Pd $3d_{5/2}$ shift with trimetallic samples, metal spectra of PdAuRh, PdAuIr, and PdAuAg. The Au 4f peak in the three trimetallic catalysts presents only metallic Au with no Au oxide detected. The same observation could be noted about Ag 3d in PdAuAg/C, Ir 4f in PdAuIr/C, and Rh 3d in PdAuRh/C. The Pd 3d is deconvoluted into low-energy band $3d_{5/2}$ and high-energy band $3d_{3/2}$, as can be seen in the Pd 3d spectrum of the four catalysts. Unlike trimetallic systems, there is a notable Pd oxide concentration in the case of the monometallic Pd/C (Fig. 4 a). Furthermore, according to Table 4, the Pd^{2+} concentration is higher (0.45 at.% %) in the case of Pd/C, followed by PdAuIr/C (0.12 at.% %). Thus, the Pd air stability is significantly enhanced in PdAuRh/C and PdAuAg/C. A similar finding regarding the effect of adding Au and Ir on Pd air stability was reported [46]. Surface compositions (at.%) are normalized to total detected elements.

Table 4 XPS metal concentration, oxidation state, peak positions of Pd/C, PdAuAg/C, PdAuIr/C, and PdAuRh/C, Binding energies (eV) referenced to C 1s at 284.8 eV

Catalyst	Pd At. %		Pd 3d (eV)	Au At. %	Au 4f (eV)	Ag At. %	Ag 3d (eV)	Ir At. %	Ir 4f (eV)	Rh At. %	Rh 3d (eV)
	Pd^0	Pd^{2+}									
Pd/C	1.63	0.45	335.43	-	-	-	-	-	-	-	-
PdAuAg/C	0.83	0.00	335.17	0.48	83.68	0.50	367.78	-	-	-	-
PdAuIr/C	0.87	0.12	335.38	0.52	83.68	-	-	1.11	61.18	-	-
PdAuRh/C	0.55	0.00	335.38	1.17	83.88	-	-	-	-	0.52	307.08

The Pd satellite peaks appear in the Pd 3d spectra of Pd/C and all trimetallic samples. It represents a loos feature that sits at a higher binding energy than the main Pd 3d doublet. These signals combine plasmon-loss (from pure Pd) and oxidized Pd species. According to the cited literature, these peaks are identical with the staelitte, and no Pd^{4+} peaks are seen. The shape, size, location, and intensity of satellite peaks differ according to oxidation degrees, alloying degree, particle size, and $NaBH_4$ metal reduction order. The total atomic EDX metal concentration is lower than its XPS counterpart, which is probably due to the surface measuring capability of XPS compared to EDX, which is more reflective of the bulk composition, according to Table 3 and Table 4. Furthermore, the highest difference between the EDX and XPS concentrations is that of PdAuIr/C, which is due to the surface segregation tendency of Ir. Similar findings have been reported [46]. It is noteworthy that PdAuAg Pd 3d is shifted 0.46 eV to a lower binding energy value compared to Pd. The binding energy position is crucial for the catalytic activity as it should strike a balance between the strength with which the catalyst could adsorb reactants and the ability to release products.

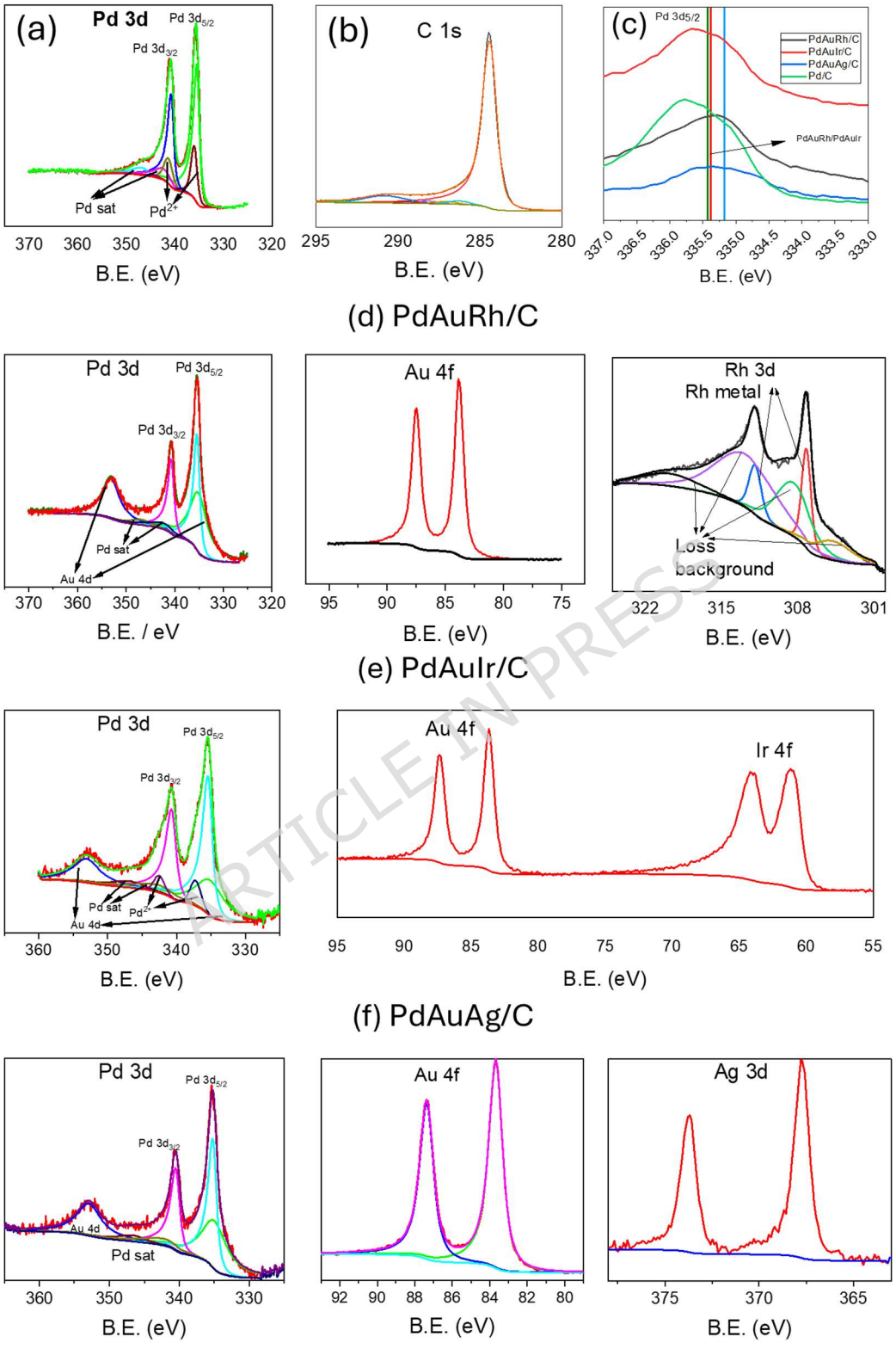

Fig. 4 XPS spectra: (a) Pd 3d in Pd/C, (b) C 1s, (c) Pd $3d_{5/2}$ binding energy shift (eV), (d) PdRhAu metal spectra, (e) PdAuIr metal spectra, (f) PdAuAg metal spectra

On the contrary to [46], the binding energy of the Pd 3d peak position of PdAuIr is 0.05 eV smaller than that of the Pd 3d of Pd/C, according to Fig. 4.c and Table *4* (the same goes to PdAuRh). A lower shift was observed in the case of Au 4f and Ag 3d compared to pure Au and Ag [67]. The shift of Au and Ag binding energies to higher values is the opposite finding of that reported by Pan *et al.* about PdAuAg/C [38, 58]. This could be due to the different synthesis methods or geometrical shapes of PdAuAg, which led to such discrepancies..

3.5. Cyclic Voltammetry (CV)

Fig. 5 (A-D) shows the cyclic voltammetry (CV) results of Pd/C, PdAuRh/C, PdAuIr/C, and PdAuAg/C in 1 M KOH (A, C) and 1 M KOH + EtOH (B, D). Fig. 5 A & B show the raw current values obtained in 1M KOH (A,C) and 1M KOH+EtOH (B, D). While Fig. 5. A & B show the raw current values obtained in 1M KOH and 1M KOH + EtOH, Fig. 5. and 1M KOH+EtOH, Fig. 5. C shows the current normalized by the GC electrode area, and Fig. 5. D shows the current normalized by the Pd weight in the electrode. All potentials are reported versus RHE. According to Fig. 5. A & C, looking at the forward scan, no H_{ads} peak is noted on Pd/C and PdAuAg/C, but it is visible on PdAuRh/C and PdAuIr/C around -150 mV vs RHE. This could only be attributed to the capability of both Ir and Rh to adsorb H species, being the only difference from Pd/C and PdAuAg/C. Similar peaks were observed for the pure Rh electrode [28] and the trimetallic PdAuIr one [7] in addition to the monometallic Ir/C [35]. Furthermore, being broad suggests the H_{ads} peak overlaps with a capacitive double-layer process, added to the fact that Pd can actually absorb hydrogen into its core structure.

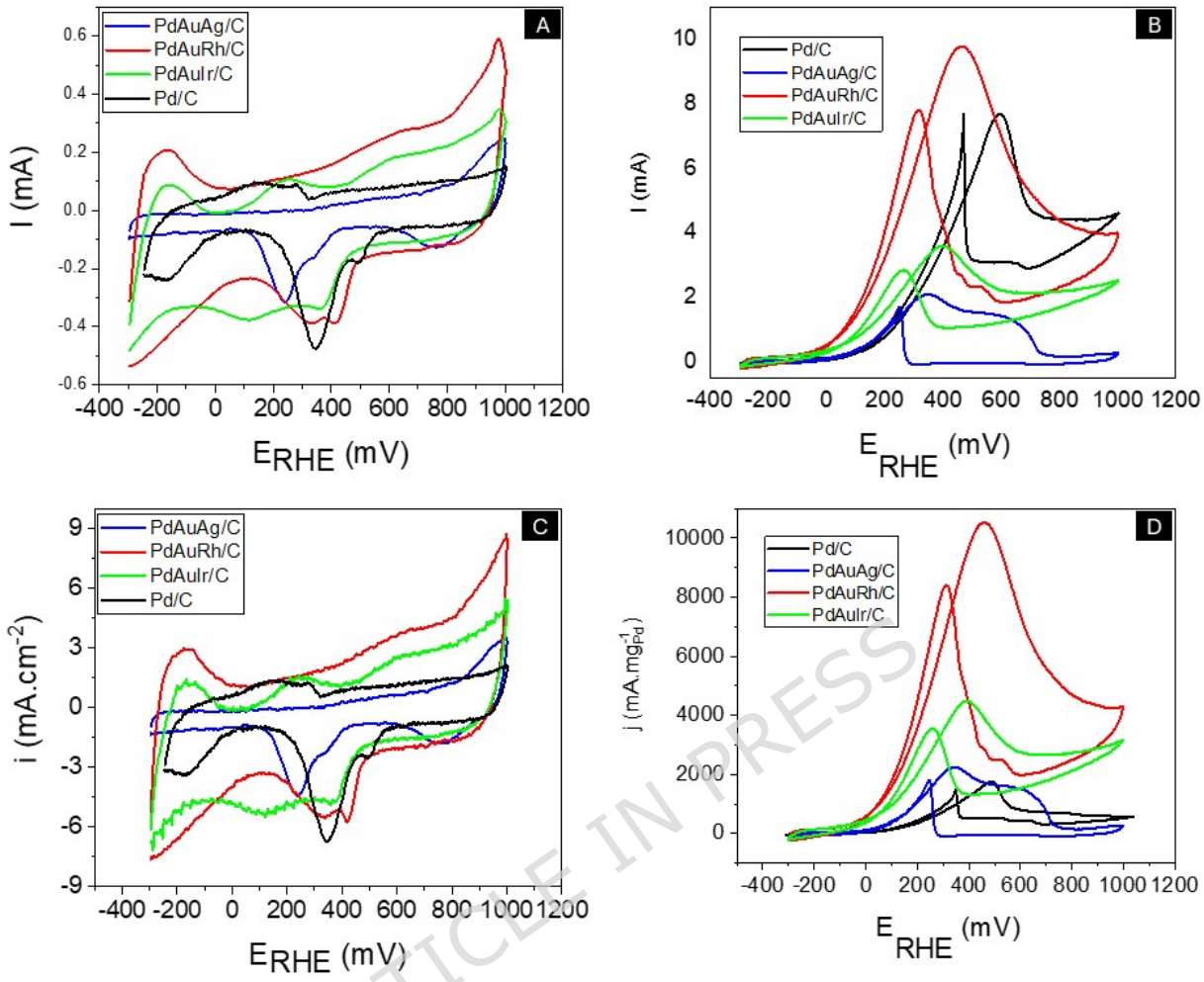

Fig. 5 Cyclic voltammetry in 1M KOH (A,C) and 1 M KOH+EtOH (B,D) at 50 mV/s of Pd/C, PdAuRh/C, PdAuIr/C, and PdAuAg/C: current normalized by electrode area (C) and Pd weight (D)

The OH adsorption occurs around +110 mV for the four samples. Above +150 mV, the Pd surface oxidation starts and continues to the end of the forward scan. During the backward scan, the Pd surface oxide is reduced to Pd metal around +275 mV as shown in Fig. 5.A & C. Furthermore, a second oxidation peak could be noted in the forward scan on PdAuRh/C (+650 mV) and PdAuIr/C (+250 mV), which are likely due to the oxidation of Rh and Ir, respectively. The monometallic Pd/C curve exhibits a PdO reduction peak around +350 mV, added to a shoulder peak at +500 mV. At the backward scan end, a broad H_{abs} peak is visible on Pd/C. Overlapping metal reduction peaks

appear on the trimetallic samples between +400 mV and +220 mV. Fig. 5. A & D show the voltammograms in 1 M KOH + 1 M KOH+EtOH in the electrochemical half-cell. The first observation is that ethanol adsorption on Pd surpassed H adsorption on all the catalysts. Upon increasing the potential to the start of the OH adsorption, a gradual increase in the current was observed. This is probably because the quantity of adsorbed OH increases with the applied potential, promoting the oxidation and removal of ethoxy species from the Pd active sites. The forward scan peak of 1800 mA/mg$_{Pd}$ - on Pd/C is located at approximately +490 mV, after which the current starts to decline due to blocking of Pd active sites. In the backward scan, a sharp peak is noted at +350 mV which is the same as the PdO reduction peak in the KOH-only voltammogram, suggesting that most of the Pd active sites were recovered, leading to further adsorption of ethanol on Pd. For Pd/C, the EOR onset potential was -85 mV. Compared to previously published monometallic Pd/C EOR data, this catalyst is a high-performing one [26, 37, 48, 64]. The addition of both Au and Rh, Ir, or Ag to Pd/C enhances its EOR performance, as shown in Fig. 5. B & D. Exceptional activity of PdAuRh/C may arise from synergistic electronic effects and minimized CO poisoning, evidenced by low onset potential (–680 mV). For instance, the EOR onset potential of PdAuAg/C has been shifted around -40 mV to the left compared with Pd/C, which implies that a lower overpotential exists against PdAuAg compared to Pd.

Furthermore, over the potential window of 0 mV to 700 mV, the Pd mass activity of PdAuAg is higher than that of Pd. Unlike PdAuRh and PdAuIr, PdAuAg shows two oxidation peaks in the forward scan at +350 mV and 600 mV vs RHE. The origin of this double peak is unclear but may reflect the oxidation of distinct intermediates (e.g., CO_{ads} and CH_3CHO). that are oxidized at two different potentials. PdAuIr achieves higher kinetic parameters than both Pd and PdAuAg, as Fig. 5. B & D show. Its EOR onset oxidation potential is approximately -400 mV (155 mV less than

that of Pd), suggesting that a smaller EOR activation barrier exists against PdAuIr. Furthermore, the oxidation current density peak was approximately twice that of Pd, suggesting high Pd surface exposure. Considering that the trimetallic $Pd_7Au_7Ir_1$/C catalyst reported by Shen et al. [46] underperformed both Pd/C and Pd_7Ir/C towards EOR, the current trimetallic PdAuIr/C catalyst exhibits remarkable performance. PdAuRh is the best-performing catalyst kinetically with the lowest EOR onset potential (-680 mV) and the highest oxidation current peak density of 10500 $mA/mg_{Pd,}$ which is more than 4 times higher than Pd and PdAuAg and 2 times higher than PdAuIr. This is very interesting since Rh is probably capable of giving a comparable performance towards EOR to that of Pd. According to De Tacconi et al. [54], who studied EOR using in-situ FTIR on both Rh and Ir surfaces, the main final product on Rh is $CO_{2,}$ while it is acetic acid on Ir surface.

3.6. Chronoamperometry (CA)

Fig. 6 shows the two-step chronoamperometry (CA) of Pd/C, PdAuAg/C, PdAuIr/C, and PdAuRh/C undertaken at +100 mV (30 min) and +500 mV (30 min) both versus RHE. These potentials were chosen because the former represents the OH adsorption window and the latter represents the potential of the Pd surface oxidation window, where the current declines due to the loss of Pd active sites. At +100 mV, the Pd/C CA current undergoes an immediate decline within the first minute to +20 mA/mg_{Pd}, which is almost constant until the end of the 30-min scan. As the lowest current density was obtained, this implies the lowest active site number on the Pd/C surface, but a very slow decline with time indicates consistent recovery of Pd active sites by removing the carbonaceous species. A similar behavior was observed for PdAuAg at the same potential. At -300 mV, the PdAuAg CA current density was slightly higher than that of Pd. At 100 mV, the situation was reversed: the Pd current density was higher than that of PdAuAg, as shown in the CV voltammogram (Fig. 5. A, C). In addition to the current density, which differed from -300 mV to

100 mV, there was also a current decline, which seemed quicker on Pd/C than at -300 mV but more stable on PdAuAg. This can be interpreted by referring to the ethanol oxidation voltammogram. For both catalysts, at -0.3V, there is a current increase due to the adsorption of OH species, and the mass activity of PdAuAg is higher than that of Pd, which is why the former CA current is slightly higher than the latter. At +0.1V, however, the CV current density of Pd is slightly higher than that of PdAuAg (Fig. 6).

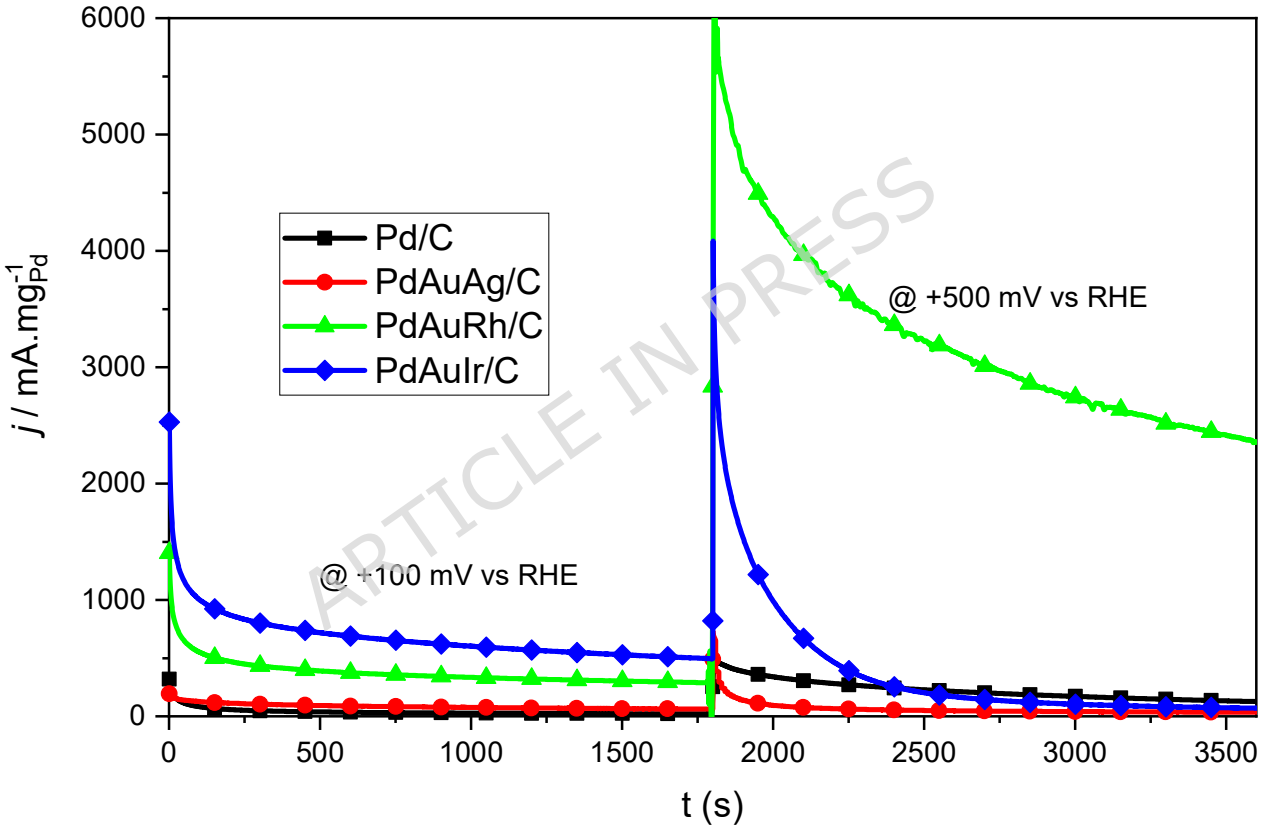

Fig. 6 Chronoamperometry (CA) scans in 1M KOH+EtOH at +100 mV and +500 mV vs RHE of Pd/C, PdAuRh/C, PdAuIr/C, and PdAuAg/C

Similar to Pd and PdAuAg, the CA current curves of PdAuIr and PdAuRh were interchangeable between +100 mV and +500 mV vs RHE. While the PdAuIr CA current was higher than that of PdAuRh/C at +100 mV, the opposite was true at +500 mV. Referring to the KOH CV (Fig. 5), it can be noted that the H absorption is more pronounced on PdAuRh than on PdAuIr, which suggests

that the PdAuRh surface is predominantly occupied by adsorbing H species more than PdAuIr. In the same figure, there is a notable current increase in PdAuIr between +100 mV and -600 mV, which could be attributed to the adsorption of OH adsorption implying that at +100 mV, there is more OH generation on PdAuIr/C than PdAuRh/C. A similar conclusion was made by Shen *et al.* [46]. That could explain the higher PdAuIr/C CA current than PdAuRh/C at +100 mV in Fig. 6. At +500 mV, however, the current obtained on PdAuRh is ≈12 times higher than that of PdAuIr/C. This suggests that PdAuRh/C is much more active towards EOR than PdAuIr/C, which was also verified by CV (Fig. 5. C & D). Both PdAuRh/C and PdAuIr/C CA currents, particularly PdAuRh, exhibit rapid current decay, indicating a rapid degradation of the Pd active sites to the extent that the PdAuIr current is lower than that of Pd after 12 min from applying + 500 mV.

3.7. Electrochemical Impedance Spectroscopy (EIS)

To test the internal impedance of the cell, electrochemical impedance spectroscopy (EIS) was performed on the trimetallic catalysts. Potentiostatic EIS experiments were performed at 100 mV and 400 mV. The frequency ranges from 10,000 Hz to 0.1 Hz, while the voltage amplitude is 5 mV. Each experiment was preceded by a 10-minute potentiostatic scan to compensate for the current perpetuation. Fig. 7 (a,b) shows the EIS spectra recorded at +100 mV and 500 mV vs RHE. The first thing to note is that increasing the potential from +100 mV to 500 mV reduces the impedance arc size, especially at low frequencies, on PdAuRh/C and PdAuIr/C, with negligible change on PdAuAg/C. This, along with the double-peak forward oxidation CV, calls for an *in-situ* investigation of the EOR mechanism and final products on PdAuAg/C. The reason for the reduction in impedance arc size is likely due to a decrease in the charge transfer resistance (R_{ct}), which is correlated with the applied potential and the abundance of OH species required to oxidize adsorbed ethoxy species.

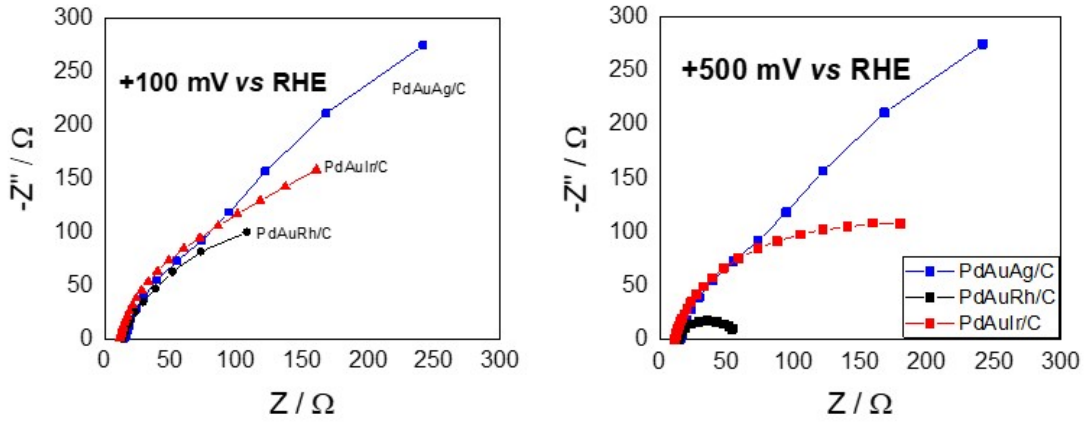

Fig. 7 Electrochemical Impedance Spectroscopy (EIS) at +100 mV (a) and +500 mV vs RHE (b) of PdAuRh/C, PdAuIr/C, and PdAuAg/C

The second notable thing is that the impedance arc size is smallest on PdAuRh/C, followed by PdAuIr/C, and finally PdAuAg/C, which substantiates that PdAuRh/C is the most active EOR trimetallic catalyst that has the lowest activation energy barrier. To draw useful numbers from the EIS scans, an electronic circuit model (Fig. 8) that is equivalent to the current 3-electrode half-cell was used. The model is comprised of solution resistance (R_s), a constant phase element (Φ) resulting from the electrode-electrolyte double layer capacitor, and the charge transfer resistance (R_{ct}), both connected in parallel. The R_s is series-connected to the R_{ct}-Φ parallel-connected pair. This model was used to fit the EIS data to estimate the R_{ct} values of each catalyst at +100 mV and 500 mV. The R_{ct} values of PdAuRh/C at 100 mV and 500 mV are approximately 280 and 45 Ω, respectively. The values obtained with PdAuIr/C are higher than those of PdAuRh/C (Table 5).

Table 5 Charge-transfer resistance (R_{ct}) values at -0.3 V and 0.0 V vs NHE on PdAuRh/C, PdAuIr/C, and PdAuAg/C

Catalyst/R_{ct}	R_{ct} Ω (@ 100 mV)	R_{ct} Ω (@ 500 mV)
PdAuAg/C	842	1091
PdAuRh/C	280	45
PdAuIr/C	377	259

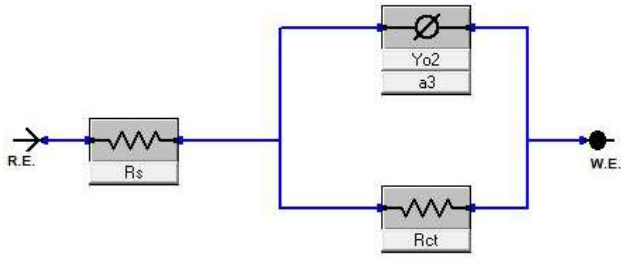

Fig. 8 Electronic model equivalent of the current 3-electrode cell reaction

4. Conclusions

Trimetallic C-supported PdAuM/C (Me = Rh, Ir, Ag) catalysts are synthesized and applied to the alkaline ethanol oxidation reaction. The addition of Au and the third metal (Rh, Ir, Ag) to Pd/C enhances its physicochemical properties (particle size, oxidation state, dispersion, and alloying potential), according to the results of XRD, TEM, EDX, and XPS. In addition, the best-performing catalyst is the PdAuRh/C, with an oxidation current peak 5.8 times higher (10,500 vs. 1,800 $mA \cdot mg^{-1}_{Pd}$) than that of its Pd/C counterpart. The lowest charge transfer resistance and oxidation onset potential were also associated with this material. The PdAuIr/C catalyst (with high alloying potential) exhibits high EOR activity, with a 2.3 times higher peak current than Pd/C. Finally, PdAuAg/C exhibited the lowest EOR performance but still outperformed Pd/C. It is noteworthy that PdAug achieves the weakest alloying between Pd, Au,. and Ag in addition to the highest binding energy shift of Pd 3d. The CV forward oxidation double-peak and EIS scans of PdAuAg/C are unusual and worthy of *in situ* investigation.

Acknowledgments

Ahmed Elsheikh is grateful for the financial support of the Newton-Mosharafa Fund (Reference no. NMJ8/15) for his Ph.D. studies.

Author Contributions

A. ElSheikh: Conceptualization, Data Curation, Methodology, Funding Acquisition, & Project administration. **H. AlSogheir**: Investigation and Manuscript Composition. **H. Mousa**: Contributed to drafting and reviewing the manuscript. C. Zhu: Data Analysis, assessment, and manuscript review. **J. McGregor**: Conceptualization, Methodology, Result analysis, and Funding Acquisition.

Funding

This work has received no external funding.

Conflict of Interests

The authors declare they have no relationships or interests that could potentially bias or influence the Manuscript.

Data Availability

The datasets used and/or analysed during the current study are available from the corresponding author on reasonable request.

Ethical Approval

Not Applicable

References

1. Akhairi MAF, Kamarudin SKK (2016) Catalysts in direct ethanol fuel cell (DEFC): An overview. Int J Hydrogen Energy 41:4214–4228. doi: 10.1016/j.ijhydene.2015.12.145

2. An L, Zhao TSS, Li YSS (2015) Carbon-neutral sustainable energy technology: Direct ethanol fuel cells. Renewable and Sustainable Energy Reviews 50:1462–1468. doi: 10.1016/j.rser.2015.05.074

3. Antolini E (2009) Carbon supports for low-temperature fuel cell catalysts. Appl Catal B 88:1–24. doi: 10.1016/J.APCATB.2008.09.030

4. Armenta-González AJ, Carrera-Cerritos R, Guerra-Balcázar M, Arriaga LG, Ledesma-García J (2015) Comparative study of carbon-supported Pd and PdAg catalysts synthesised by the polyol process and reverse micelles methods. J Appl Electrochem 45:33–41. doi: 10.1007/s10800-014-0776-x

5. Assumpção MHMT, Da Silva SG, De Souza RFB, Buzzo GS, Spinacé E V., Santos MC, Neto AO, Silva JCM (2014) Investigation of PdIr/C electrocatalysts as anode on the performance of direct ammonia fuel cell. J Power Sources 268:129–136. doi: 10.1016/j.jpowsour.2014.06.025

6. Bianchini C, Shen PK (2009) Palladium-based electrocatalysts for alcohol oxidation in half cells and in direct alcohol fuel cells. Chem Rev 109:4183–4206. doi: 10.1021/cr9000995

7. Brandalise M (2008) Preparation and characterization of electrocatalysts based on palladium for electro-oxidation of alcohols in alkaline medium

8. Chen LY, Chen N, Hou Y, Wang ZC, Lv SH, Fujita T, Jiang JH, Hirata A, Chen MW (2013) Geometrically Controlled Nanoporous PdAu Bimetallic Catalysts with Tunable Pd/Au Ratio for Direct Ethanol Fuel Cells. ACS Catal 3:1220–1230. doi: 10.1021/cs400135k

9. Christensen PA, Jones SWM, Hamnett A (2012) In Situ FTIR Studies of Ethanol Oxidation at Polycrystalline Pt in Alkaline Solution. The Journal of Physical Chemistry C 116:24681–24689. doi: 10.1021/jp308783y

10. Dutta A, Datta J (2012) Outstanding Catalyst Performance of PdAuNi Nanoparticles for the Anodic Reaction in an Alkaline Direct Ethanol (with Anion-Exchange Membrane) Fuel Cell. The Journal of Physical Chemistry C 116:25677–25688. doi: 10.1021/jp305323s

11. Dutta A, Mondal A, Broekmann P, Datta J (2017) Optimal level of Au nanoparticles on Pd nanostructures providing remarkable electro-catalysis in direct ethanol fuel cell. J Power Sources 361:276–284. doi: 10.1016/J.JPOWSOUR.2017.06.063

12. Dutta A, Mondal A, Broekmann P, Datta J (2017) Optimal level of Au nanoparticles on Pd nanostructures providing remarkable electro-catalysis in direct ethanol fuel cell. J Power Sources 361:276–284. doi: 10.1016/J.JPOWSOUR.2017.06.063

13. Elsheikh A, McGregor J (2021) Synthesis and characterization of pdagni/c trimetallic nanoparticles for ethanol electrooxidation. Nanomaterials 11. doi: 10.3390/nano11092244

14. Elsheikh A, Torrero J, Rojas S, McGregor J (2023) In-situ FTIR spectroscopy investigation of carbon-supported PdAuNi electrocatalysts for ethanol oxidation. Journal of Electroanalytical Chemistry 928:116985. doi: 10.1016/j.jelechem.2022.116985

15. Elsheikh AMA, Backović G, Oliveira RCP, Sequeira CAC, McGregor J, Šljukić B, Santos DMF (2021) Carbon-supported trimetallic catalysts (Pdauni/c) for borohydride oxidation reaction. Nanomaterials 11. doi: 10.3390/nano11061441

16. Feng J, Liu Y, Yin M, He Y, Zhao J, Sun J, Li D (2016) Preparation and structure-property relationships of supported trimetallic PdAuAg catalysts for the selective hydrogenation of acetylene. J Catal 344:854–864. doi: 10.1016/j.jcat.2016.08.003

17. Feng Y-Y, Liu Z-H, Xu Y, Wang P, Wang W-H, Kong D-S (2013) Highly active PdAu alloy catalysts for ethanol electro-oxidation. J Power Sources 232:99–105. doi: 10.1016/j.jpowsour.2013.01.013

18. Feng Y-Y, Liu Z-H, Xu Y, Wang P, Wang W-H, Kong D-S (2013) Highly active PdAu alloy catalysts for ethanol electro-oxidation. J Power Sources 232:99–105. doi: 10.1016/j.jpowsour.2013.01.013

19. Fontes EH, Nandenha J, Piasentin RM, Souza RFB De (2020) Comparison of various atomic compositions of Au @ Pd / C , Pd / C , and AuPd / C electrocatalysts for direct ethanol fuel cells. 1–15. doi: 10.1002/est2.139

20. Gao F, Yin Y, Cao Z, Li H, Guo P (2020) Synthesis of Bimetallic PdAg Nanoparticles and Their Electrocatalytic Activity toward Ethanol. J Chem 2020. doi: 10.1155/2020/1917380

21. Geraldes AN, Furtunato Da Silva D, Martins da Silva JC, Antonio de Sá O, Spinacé EV, Neto AO, Coelho dos Santos M (2015) Palladium and palladium–tin supported on multi wall carbon nanotubes or carbon for alkaline direct ethanol fuel cell. J Power Sources 275:189–199. doi: 10.1016/J.JPOWSOUR.2014.11.024

22. Geraldes AN, da Silva DF, Pino ES, da Silva JCM, de Souza RFB, Hammer P, Spinacé EV, Neto AO, Linardi M, dos Santos MC (2013) Ethanol electro-oxidation in an alkaline medium using Pd/C, Au/C and PdAu/C electrocatalysts prepared by electron beam irradiation. Electrochim Acta 111:455–465. doi: 10.1016/j.electacta.2013.08.021

23. Geraldes AN, da Silva DF, Pino ES, da Silva JCM, de Souza RFB, Hammer P, Spinacé EV, Neto AO, Linardi M, dos Santos MC (2013) Ethanol electro-oxidation in an alkaline

medium using Pd/C, Au/C and PdAu/C electrocatalysts prepared by electron beam irradiation. Electrochim Acta 111:455–465. doi: 10.1016/j.electacta.2013.08.021

24. Henrique RS, Ayoub JMS, Piasentin RM, Linardi M, Santos MC (2012) Preparation of Pt / C-In 2 O 3 . SnO 2 Electrocatalysts by Borohydride Reduction Process for Ethanol Electro-Oxidation. Int J Electrochem Sci 7:2036–2046. doi: 10.1007/s11581-013-0955-5

25. Hosseini MG, Abdolmaleki M (2013) Synthesis and characterization of porous nanostructured Ni/PdNi electrode towards electrooxidation of borohydride. Int J Hydrogen Energy 38:5449–5456. doi: 10.1016/j.ijhydene.2012.09.051

26. Hu G, Nitze F, Reza Barzegar H, Sharifi T, Mikołajczuk A, Tai C-W, Borodzinski A, Wågberg T (2012) Palladium nanocrystals supported on helical carbon nanofibers for highly efficient electro-oxidation of formic acid, methanol and ethanol in alkaline electrolytes. J Power Sources 209:236–242. doi: 10.1016/j.jpowsour.2012.02.080

27. Lam BTX, Chiku M, Higuchi E, Inoue H (2015) Preparation of PdAg and PdAu nanoparticle-loaded carbon black catalysts and their electrocatalytic activity for the glycerol oxidation reaction in alkaline medium. J Power Sources 297:149–157. doi: 10.1016/J.JPOWSOUR.2015.07.086

28. Lazarova Y, Dodevska T (2018) Amperometric sensing of hydrogen peroxide using glassy carbon electrode modified with rhodium. Food Science and Applied Biotechnology 1:63–69. doi: 10.30721/fsab2018.v1.i1

29. Liu C-H, Liu R-H, Sun Q-J, Chang J-B, Gao X, Liu Y, Lee S-T, Kang Z-H, Wang S-D (2015) Controlled synthesis and synergistic effects of graphene-supported PdAu bimetallic

nanoparticles with tunable catalytic properties. Nanoscale 7:6356–6362. doi: 10.1039/C4NR06855F

30. Ma L, Chu D, Chen R (2012) Comparison of ethanol electro-oxidation on Pt/C and Pd/C catalysts in alkaline media. Int J Hydrogen Energy 37:11185–11194. doi: 10.1016/j.ijhydene.2012.04.132

31. Maksić A, Smiljanić M, Miljanić Š, Rakočević Z, Štrbac S (2016) Ethanol Oxidation on Rh/Pd(poly) in Alkaline Solution. Electrochim Acta 209:323–331. doi: 10.1016/J.ELECTACTA.2016.05.096

32. Moraes LPR, Matos BR, Radtke C, Santiago EI, Fonseca FC, Amico SC, Malfatti CF (2016) Synthesis and performance of palladium-based electrocatalysts in alkaline direct ethanol fuel cell. Int J Hydrogen Energy 41:6457–6468. doi: 10.1016/j.ijhydene.2016.02.150

33. Neto AO, Nandenha J, De Souza RFB, Buzzo GS, Silva JCM, Spinacé EV, Assumpção MHMT (2014) Anodic oxidation of formic acid on PdAuIr/C-Sb2O5·SnO2 electrocatalysts prepared by borohydride reduction. Journal of Fuel Chemistry and Technology 42:851–857. doi: 10.1016/S1872-5813(14)60037-2

34. Neto AO, Da Silva SG, Buzzo GS, De Souza RFB, Assumpção MHMT, Spinacé E V, Silva JCM Ethanol electrooxidation on PdIr/C electrocatalysts in alkaline media: electrochemical and fuel cell studies. doi: 10.1007/s11581-014-1201-5

35. Neto AO, Da Silva SG, Buzzo GS, De Souza RFB, Assumpção MHMT, Spinacé E V, Silva JCM Ethanol electrooxidation on PdIr/C electrocatalysts in alkaline media: electrochemical and fuel cell studies. doi: 10.1007/s11581-014-1201-5

36. Neto AO, Tusi MM, De Oliveira Polanco NS, Da Silva SG, Coelho Dos Santos M, Spinacé E V. (2011) PdBi/C electrocatalysts for ethanol electro-oxidation in alkaline medium. Int J Hydrogen Energy 36:10522–10526. doi: 10.1016/j.ijhydene.2011.05.154

37. Obradović MD, Stančić ZM, Lačnjevac UČ, Radmilović VVVR, Gavrilović-Wohlmuther A, Radmilović VVVR, Gojković SLj (2016) Electrochemical oxidation of ethanol on palladium-nickel nanocatalyst in alkaline media. Appl Catal B 189:110–118. doi: 10.1016/J.APCATB.2016.02.039

38. Pan B, Chen F, Kou B, Wang J, Tang Q, Guo L, Wang Q, Li Z, Bian W, Wang J (2020) Unexpectedly high stability and surface reconstruction of PdAuAg nanoparticles for formate oxidation electrocatalysis. Nanoscale 12:11659–11671. doi: 10.1039/d0nr01358g

39. Pech-Rodríguez WJJ, González-Quijano D, Vargas-Gutiérrez G, Morais C, Napporn TWW, Rodríguez-Varela FJJ (2017) Electrochemical and in situ FTIR study of the ethanol oxidation reaction on PtMo/C nanomaterials in alkaline media. Appl Catal B 203:654–662. doi: 10.1016/j.apcatb.2016.10.058

40. Qi J, Benipal N, Liang C, Li W (2016) PdAg/CNT catalyzed alcohol oxidation reaction for high-performance anion exchange membrane direct alcohol fuel cell (alcohol = methanol, ethanol, ethylene glycol and glycerol). Appl Catal B 199:494–503. doi: 10.1016/j.apcatb.2016.06.055

41. Qin Y-H, Jiang Y, Niu D-F, Zhang X-S, Zhou X-G, Niu L, Yuan W-K (2012) Carbon nanofiber supported bimetallic PdAu nanoparticles for formic acid electrooxidation. J Power Sources 215:130–134. doi: 10.1016/J.JPOWSOUR.2012.05.008

42. Qin Y-H, Jiang Y, Niu D-F, Zhang X-S, Zhou X-G, Niu L, Yuan W-K (2012) Carbon nanofiber supported bimetallic PdAu nanoparticles for formic acid electrooxidation. J Power Sources 215:130–134. doi: 10.1016/J.JPOWSOUR.2012.05.008

43. Sheikh AM, Silva EL, Correa PS, Menezes TL (2014) The Effect of Adding Ni and Sn to Pd Catalysts on the Direct Ethanol Fuel Cell Performance. In: 2014 International Conference on Energy, Environment and Materials Engineering (EEME 2014)

44. Sheikh AM, Silva EL, Moares L, Antonini LM, Abellah MY, Malfatti CF (2014) Pd-based Catalysts for Ethanol Oxidation in Alkaline Electrolyte. 2:64–69. doi: 10.12691/ajmm-2-4-1

45. Shen S, Zhao TS, Xu J, Li Y (2011) High performance of a carbon supported ternary PdIrNi catalyst for ethanol electro-oxidation in anion-exchange membrane direct ethanol fuel cells. Energy Environ Sci 4:1428. doi: 10.1039/c0ee00579g

46. Shen SY, Guo YG, Wei GH, Luo LX, Li F, Zhang JL A perspective on the promoting effect of Ir and Au on Pd toward the ethanol oxidation reaction in alkaline media. doi: 10.1007/s11708-018-0586-7

47. Shen SY, Zhao TS, Xu JB (2010) Carbon-supported bimetallic PdIr catalysts for ethanol oxidation in alkaline media. Electrochim Acta 55:9179–9184. doi: 10.1016/j.electacta.2010.09.018

48. Sikeyi LL, Matthews T, Adekunle AS, Maxakato NW (2020) Electro-oxidation of Ethanol and Methanol on Pd/C, Pd/CNFs and Pd−Ru/CNFs Nanocatalysts in Alkaline Direct Alcohol Fuel Cell. Electroanalysis 32:2681–2692. doi: 10.1002/elan.202060260

49. Da Silva EL, Ortega Vega MR, Correa PDS, Cuña A, Tancredi N, Malfatti CDF (2014) Influence of activated carbon porous texture on catalyst activity for ethanol electro-oxidation. Int J Hydrogen Energy 39:14760–14767. doi: 10.1016/j.ijhydene.2014.07.103

50. da Silva SG, Assumpção MHMT, Silva JCM, De Souza RFB, Spinacé E V., Neto AO, Buzzo GS (2014) PdSn/C electrocatalysts with different atomic ratios for ethanol electro-oxidation in alkaline media. Int J Electrochem Sci 9

51. Su PP-C, Chen H-SH, Chen TT-Y, Liu C-WC, Lee C-H, Lee J-F, Chan T-S, Wang K-W (2013) Enhancement of electrochemical properties of Pd/C catalysts toward ethanol oxidation reaction in alkaline solution through Ni and Au alloying. Int J Hydrogen Energy 38:4474–4482. doi: 10.1016/J.IJHYDENE.2013.01.173

52. Suo Y, Hsing I (2011) Synthesis of bimetallic PdAu nanoparticles for formic acid oxidation. Electrochim Acta 56:2174–2183. doi: 10.1016/j.electacta.2010.12.037

53. Suo Y, Hsing I (2011) Synthesis of bimetallic PdAu nanoparticles for formic acid oxidation. Electrochim Acta 56:2174–2183. doi: 10.1016/j.electacta.2010.12.037

54. De Tacconi NR, Lezna RO, Beden B, Hahn F, Lamy C (1994) In-situ FTIR study of the electrocatalytic oxidation of ethanol at iridium and rhodium electrodes

55. Ulas B, Caglar A, Sahin O, Kivrak H (2018) Composition dependent activity of PdAgNi alloy catalysts for formic acid electrooxidation. J Colloid Interface Sci 532:47–57. doi: 10.1016/j.jcis.2018.07.120

56. Wang C, Song P, Gao F, Song T, Zhang Y, Chen C, Li L, Jin L, Du Y (2019) Precise synthesis of monodisperse PdAg nanoparticles for size-dependent electrocatalytic oxidation reactions. J Colloid Interface Sci 544:284–292. doi: 10.1016/j.jcis.2019.02.066

57. Xu C, Chen Q, Ding R, Huang S, Zhang Y, Fan G (2021) Sustainable solid-state synthesis of uniformly distributed PdAg alloy nanoparticles for electrocatalytic hydrogen oxidation and evolution. Chinese Journal of Catalysis 42:251–258. doi: 10.1016/S1872-2067(20)63650-6

58. Xu H, Wang J, Yan B, Li S, Wang C, Shiraishi Y, Yang P, Du Y (2017) Facile construction of fascinating trimetallic PdAuAg nanocages with exceptional ethylene glycol and glycerol oxidation activity. Nanoscale 9:17004–17012. doi: 10.1039/c7nr06737b

59. Xu H, Yan B, Zhang K, Wang C, Zhong J, Li S, Du Y, Yang P (2017) PVP-stabilized PdAu nanowire networks prepared in different solvents endowed with high electrocatalytic activities for the oxidation of ethylene glycol and isopropanol. Colloids Surf A Physicochem Eng Asp 522:335–345. doi: https://doi.org/10.1016/j.colsurfa.2017.03.015

60. Yin Z, Chi M, Zhu Q, Ma D, Sun J, Bao X (2013) Supported bimetallic PdAu nanoparticles with superior electrocatalytic activity towards methanol oxidation. J Mater Chem A Mater 1:9157. doi: 10.1039/c3ta11592c

61. Yu-Chen Wei, Chen-Wei Liu, Wei-Da Kang, Chien-Ming Lai, Li-Duan Tsai K-WW (2011) Electro-catalytic activity enhancement of Pd–Ni electrocatalysts for the ethanol electro-oxidation in alkaline medium: The promotional effect of CeO2 addition. Journal of Electroanalytical Chemistry 660:64–70. doi: 10.1016/J.JELECHEM.2011.06.006

62. Zhang G, Wang Y, Wang X, Chen Y, Zhou Y, Tang Y, Lu L, Bao J, Lu T (2011) Preparation of Pd – Au / C catalysts with different alloying degree and their electrocatalytic performance for formic acid oxidation. Appl Catal B 102:614–619. doi: 10.1016/j.apcatb.2010.12.049

63. Zhang S, Qing M, Zhang H, Tian Y (2009) Electrocatalytic oxidation of formic acid on functional MWCNTs supported nanostructured Pd–Au catalyst. Electrochem commun 11:2249–2252. doi: 10.1016/J.ELECOM.2009.10.001

64. Zhang Z, Xin L, Sun K, Li W (2011) Pd–Ni electrocatalysts for efficient ethanol oxidation reaction in alkaline electrolyte. Int J Hydrogen Energy 36:12686–12697. doi: 10.1016/j.ijhydene.2011.06.141

65. Zhou ZY, Wang Q, Lin JL, Tian N, Sun SG (2010) In situ FTIR spectroscopic studies of electrooxidation of ethanol on Pd electrode in alkaline media. Electrochim Acta 55:7995–7999. doi: 10.1016/j.electacta.2010.02.071

66. Zhu C, Wen D, Oschatz M, Holzschuh M, Liu W, Herrmann A-KK, Simon F, Kaskel S, Eychmüller A (2015) Kinetically controlled synthesis of PdNi bimetallic porous nanostructures with enhanced electrocatalytic activity. Small 11:1430–1434. doi: 10.1002/smll.201401432

67. Thermo Scientific X-ray Photoelectron Spectroscopy XPS. https://xpssimplified.com/index.php. Accessed 15 Aug 2019